

Survey2Survey: A deep learning generative model approach for cross-survey image mapping

Brandon Buncher¹[★], Awshesh Nath Sharma² and Matias Carrasco Kind^{3,4,5}

¹*Department of Physics, University of Illinois, Champaign, IL 61820 USA*

²*Department of Earth Sciences, Indian Institute of Technology Roorkee, Roorkee, Uttarakhand 247667 India*

³*Department of Astronomy, University of Illinois, Urbana, IL 61801 USA*

⁴*National Center for Supercomputing Applications, Urbana, IL 61801 USA*

⁵*Center for Astrophysical Surveys, Urbana, IL 61801 USA*

7 April 2021

ABSTRACT

During the last decade, there has been an explosive growth in survey data and deep learning techniques, both of which have enabled great advances for astronomy. The amount of data from various surveys from multiple epochs with a wide range of wavelengths and vast sky coverage, albeit with varying brightness and quality, is overwhelming, and leveraging information from overlapping observations from different surveys has limitless potential in understanding galaxy formation and evolution. Synthetic galaxy image generation using physical models has been an important tool for survey data analysis, while using deep learning generative models shows great promise. In this paper, we present a novel approach for robustly expanding and improving survey data through cross-survey feature translation. We trained two types of generative neural networks to map images from the Sloan Digital Sky Survey (SDSS) into corresponding images from the Dark Energy Survey (DES), increasing the brightness and S/N of the fainter, lower quality source images without losing important morphological information. We demonstrate the robustness of our method by generating DES representations of SDSS images from outside the overlapping region, showing that the brightness and quality are improved even when the source images are of lower quality than the training images. Finally, we highlight several images in which the reconstruction process appears to have removed large artifacts from SDSS images. While only an initial application, our method shows promise as a method for robustly expanding and improving the quality of optical survey data and provides a potential avenue for cross-band reconstruction.

Key words: galaxies: – surveys – deep learning – methods: data analysis – aperture photometry

1 INTRODUCTION

The analysis of optical data at a wide frequency range collected by various astronomical surveys is a critical component used to study the origin and evolution of galaxies. Data on galaxy shape (Wang et al. 2019) and luminosity (Padmanabhan & Loeb 2020; Cortese et al. 2017) in various bands provide information about the evolution of galaxies at different cosmic times. As each band provides information about different characteristics of each object stronger conclusions may be drawn from studies that incorporate data from a wide range of wavelengths. While a large range of optical wavelengths is covered by most modern surveys (e.g.

DES, SDSS, LSST), the depth, the footprint, and signal-to-noise ratio (S/N) varies from survey to survey. As a result, feature extraction in a particular band may be difficult in certain regions due to incomplete field coverage by surveys with high-quality data within that band.

In order to understand the underlying galaxy formation model and physics behind galaxy properties, simulations are required to mimic observations and their systematics which is computationally expensive.

Synthetic image generation of individual objects via deep learning is an alternative method for synthetic sky catalog generation that avoids the time and computational expense of other physically driven simulations. Various neural network architectures have been used for this purpose, including variational autoencoders (Regier et al. 2015a; Regier

[★] buncher2@illinois.edu

et al. 2015b; Lanusse et al. 2020) and generative adversarial networks (GANs) (Smith & Geach 2019). While these methods efficiently generate mock galaxy images, the accuracy of the output images depends on that of the input images. As a result, their physical information is fundamentally limited by the quality of the survey data they are initialized with. False image generation can also be achieved without deep learning using methods such as `GalSim` (Rowe et al. 2015), which generates false images through semi-analytic forward modelling of the image capture process; however, these methods require prior knowledge of various observables of the objects being modelled.

One unexplored alternative for improving the size and quality of survey datasets is through the use of feature transfer techniques across survey data. A feature transfer model is trained to recognize differences between features in corresponding image pairs \mathcal{X} and \mathcal{Y} from datasets \mathbb{X} and \mathbb{Y} . Using an image from $\mathcal{X}' \in \mathbb{X}$ as input, the trained neural network can then be used to construct a representation of this image with the features characteristic of images in \mathbb{Y} .

Methods other than feature transfer ones can be used to generate representations of galaxies with altered parameters. In particular, fader networks (Lample et al. 2017; Perarnau et al. 2016) have been used by Schawinski et al. (2018) for the purpose of hypothesis testing. While this could be used as a method to transfer individual physical parameters of galaxies from one dataset to another, full cross-survey image reconstruction would not be feasible using this method because of the large number of parameters that must be altered to generate faithful representations of images in the target dataset.

We propose a novel method of feature transfer between galaxy surveys using AECNNs and CycleGANs that can be used to expand galaxy image catalogs and can be adopted to multiple wavelengths and resolutions. By initializing these architectures with images from DES DR1 (Abbott et al. 2018) and SDSS DR16 (Ahumada et al. 2020), we demonstrate that information from DES images may be transferred to SDSS images, improving their S/N, contrast, and brightness. We show that the synthetic DES images reconstructed from SDSS images share the same characteristics as the true DES images, and that this consistency is retained when performing reconstructions using images from a separate set of lower quality SDSS images which do not have a counterpart in the DES catalog.

In this work, we demonstrate the creation of `Survey2Survey`, a neural network architecture used to transfer features between SDSS and DES galaxy images that can be easily generalized to other optical surveys or even across multiple wavelengths. The parameters of the SDSS and DES datasets used for training and validation are described in Section 2. In Section 3, we detail the AECNN and CycleGAN architectures used. In Section 4, we present qualitative and quantitative metrics of the accuracy of the reconstructed image, then summarize our findings in Section 5.

2 DATA

In this section we describe the datasets used to carry out this study. We focused on optical data from the SDSS and DES surveys and the overlapping region in the Stripe82 (Jiang

et al. 2014a). All of the data used in this paper is publicly accessible via their respective websites.

All images consisted of three layers (one layer for each R, G, B channel), where the brightness of each pixel P_i was represented by an 8-bit integer (i.e. $0 \leq P_i \leq 255$); each SDSS image was 150×150 pix, and each DES image was 228×228 pix. After the reconstruction and prior to the analysis, each each image was reduced to a single 150×150 pix layer by averaging over the R, G, B channels.

SDSS

SDSS images were been captured by the Ritchey-Chrétien altitude-azimuth telescope (Gunn et al. 2006), the Irène du Pont Telescope (Bowen & Vaughan 1973), and the NMSU 1-Meter Telescope (Holtzman et al. 2010). We selected a sample of galaxies in Stripe82 that overlapped with the DES footprint, and randomly sampled data from outside that region and within the northern cap for a total of 25,000 galaxies. We chose galaxies with band Petrosian magnitude limits $14 < R < 17.77$, $z < 0.25$ and a resolution of 0.396 arcsec/pix, using the galaxy flag produced by SDSS to select high confidence galaxy images. Images of these galaxies were obtained from the SDSS cutout server¹.

DES and Overlap Region

DES uses the Dark Energy Camera (DECam; Flaugher et al. 2015) mounted at the Blanco 4m telescope at the Cerro Tololo Inter-American Observatory (CTIO) in Chile to observe $\sim 5000 \text{ deg}^2$ of the southern sky in the g, r, i, z , and Y broadband filters ranging from $\sim 400 \text{ nm}$ to $\sim 1000 \text{ nm}$ in wavelength.

We used images from the Dark Energy Survey DR1 release (Abbott et al. 2018), which is comprised of over 10,000 co-added tiles of 0.534 deg^2 with a resolution of 0.263 arcsec/pix and a depth reaching $S/N \sim 10$ for extended objects up to $i_{AB} \sim 23.1$.

We selected DES galaxies using a combination of filtered criteria in terms of the concentration and error in the magnitude model as recommended² with $g < 17$ located in the Stripe 82 region (Jiang et al. 2014a) corresponding to roughly 300 deg^2 near the celestial equator. We selected all images from Stripe 82 that have an SDSS counterpart (Abazajian et al. 2009; Jiang et al. 2014b). These images were obtained using the public DES cutout service³. We removed images with incomplete coverage and cleaned the images of anomalies and contaminants such as stars using visual inspection. Each DES image was scaled to 150×150 pix to match the resolution of the SDSS images. We aligned the orientation and central pixels of each DES/SDSS image pair, and the final RGB composite was generated using the Lupton et al. (2004) prescription in order to closely match the SDSS colors. Figure 1 shows examples of the galaxies selected where we can see that the DES images exhibit a higher signal-to-noise ratio than the SDSS images.

The overlap region was used for training and validation;

¹ <http://casjobs.sdss.org/ImgCutoutDR7>

² <https://des.ncsa.illinois.edu/releases/dr1/dr1-faq>

³ <https://des.ncsa.illinois.edu/desaccess>

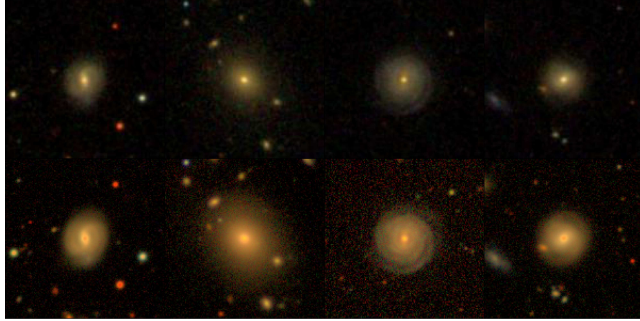


Figure 1: Sample images used from the Dark Energy Survey (DES) (top row) and Sloan Digital Sky Survey (SDSS) (bottom row) datasets. More examples can be seen throughout the text.

each SDSS image in the overlap region had a DES counterpart. In total, there were 5,538 R, G, B images in the overlap region. 5,000 SDSS/DES image pairs were used for training the models, while the remaining 538 were used as the validation dataset.

3 METHODOLOGY

Convolutional Autoencoders (AECNN) (Bepler et al. 2019) and Cycle-Consistent Generative Adversarial Networks (CycleGAN) (Durugkar et al. 2016) were used to generate synthetic galaxy images from the SDSS input images. Since the images were scaled, rotated, and centered so that each pair of pixels in a given image pair corresponded with one another, optimizing the loss function used for both models corresponded with minimizing the pixel-to-pixel differences between the reconstructed image and the DES target image. These two types of models differ in their implementation and objective function as described below.

3.1 Deep Convolutional Autoencoders (AECNN)

The architecture of a Deep Convolutional Autoencoder (AECNN) is designed to iteratively calculate a set of convolution filters that isolate important features from an input image to a representation of a target image with minimal differences between the images. Our architecture is shown in Table 1; for details about the general architecture used for AECNNs, see (Bepler et al. 2019; Li et al. 2018).

The R, G, B data from each image was separated into three layers, each of which were used to generate a unique set of filters. The encoder and decoder both consisted of three hidden layers, each of which filtered the image data from the previous layer using 150 3×3 pix convolution filters. These filters were initialized using randomly generated weights. Rectified Linear Unit (ReLU) activation functions were used for each layer of the encoder and decoder, and a sigmoid activation function was used during the final reconstruction phase. For each epoch, the input image \mathbf{x}_0 was an image from the SDSS catalog, while the target image \mathbf{x}_T was the same object taken from the DES catalog. The difference between the reconstructed image and the target image was calculated using the mean squared error loss function

Layer Type	Activation	\mathbb{D}_F	N_P
Downsampling	ReLU	128	3584
Downsampling	ReLU	64	73792
Downsampling	ReLU	32	18464
Upsampling	ReLU	32	9248
Upsampling	ReLU	64	18496
Upsampling	ReLU	128	73856
Decoding	Sigmoid	3	3459

Table 1: AECNN architecture used for image reconstruction. The input and output images were 150×150 pix with 3 color channels. Each layer used a 3×3 convolution to down- or up-sample the image. \mathbb{D}_F is the output dimensionality of the layer and N_P is the number of training features in that layer.

$$\mathcal{L}(\mathbf{x}'_0, \mathbf{x}_T) = \|\mathbf{x}_T - \mathbf{x}'_0\| \quad (1)$$

$$= \|\mathbf{x}'_T - \sigma'(\mathbf{W}'\sigma(\mathbf{W}\mathbf{x} + \mathbf{b}) + \mathbf{b}')\| \quad (2)$$

The **Adadelta** (Zeiler 2012) optimizer was used to determine filter weights. At the conclusion of 500 training epochs, the trained algorithm was used to reconstruct the DES validation images from their corresponding SDSS image.

3.2 Cycle Generative Adversarial Networks (CycleGAN)

A Generative Adversarial Network (GAN) (Durugkar et al. 2016) is an unsupervised or semi-supervised generative model consisting of a generator G and discriminator D . D is trained to distinguish between images from a training dataset of “true” images (\mathcal{Y}) and those generated by sampling from the latent space of G (\mathcal{X}). Backpropagation of error from D is used to generate a map $g : \mathcal{X} \rightarrow \mathcal{Y}$ from the latent space of G to the “true” image dataset by minimizing a loss function $\mathcal{L}(G, D, \mathcal{X}, \mathcal{Y})$. After training, the GAN may be used to generate false images that replicate the features of \mathcal{Y} .

A CycleGAN (Zhu et al. 2017; Isola et al. 2017) is a variation of a traditional GAN that minimizes cycle-consistency loss through the addition of a second generator/discriminator pair; a diagram of this architecture is shown in Figure 2. Images from \mathcal{X} (\mathcal{Y}) are used to train discriminators $D_{\mathcal{X}}$ ($D_{\mathcal{Y}}$). The generators $F : \mathcal{X} \rightarrow \mathcal{Y}$ and $G : \mathcal{Y} \rightarrow \mathcal{X}$ are trained to extremize the adversarial loss function $\mathcal{L}(H, D_{\mathcal{Y}}, \mathcal{U}, \mathcal{V})$ for generator H , discriminator $D_{\mathcal{V}}$, and datasets \mathcal{U} and \mathcal{V} . For the purposes of this project, we chose to use the loss function used by Zhu et al. (2017):

$$\mathcal{L}_{\text{GAN}}(H, D_{\mathcal{V}}, \mathcal{U}, \mathcal{V}) = \mathbb{E}_{y \sim p_{\text{data}}(y)} [\log D_{\mathcal{V}}(y)] + \mathbb{E}_{x \sim p_{\text{data}}} [\log(1 - D_{\mathcal{V}}(G(x)))] \quad (3)$$

For images $x \in \mathcal{X}$ and $y \in \mathcal{Y}$, where p_{data} is the true data distribution. G was trained to maximize $\mathcal{L}_{\text{GAN}}(\max_G \max_{D_{\mathcal{Y}}} \mathcal{L}_{\text{GAN}}(G, D_{\mathcal{Y}}, \mathcal{X}, \mathcal{Y}))$, while F was trained to minimize it ($\min_F \max_{D_{\mathcal{X}}} \mathcal{L}_{\text{GAN}}(F, D_{\mathcal{X}}, \mathcal{Y}, \mathcal{X})$).

To constrain the space of possible mapping functions, a CycleGAN optimizes F and G by minimizing the forward and backward cycle consistency error. For images $x \in \mathcal{X}$ and $y \in \mathcal{Y}$, let $x' = F(G(x))$ and $y' = G(F(y))$. Forward

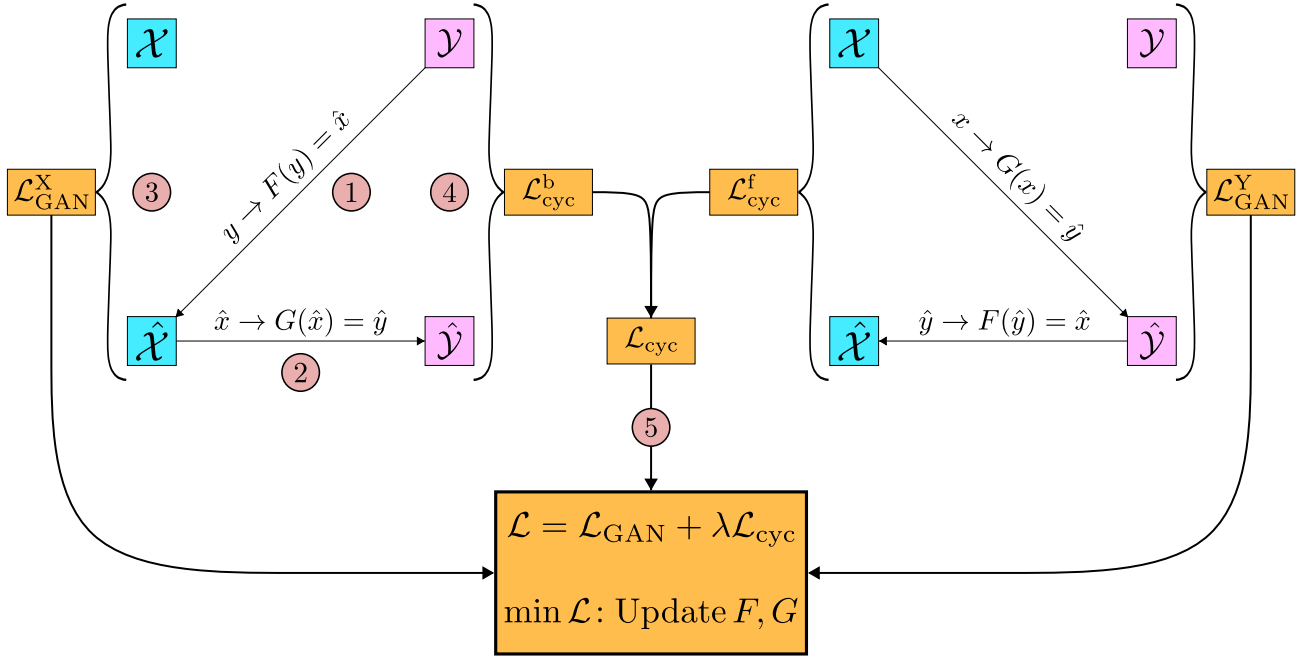


Figure 2: A representation of the architecture of a CycleGAN. **1.** A false image representation \hat{x} is generated from y , a member of the target dataset, via the mapping function F . **2.** \hat{x} is mapped to a false image \hat{y} via the mapping function G . **3.** The GAN loss function $\mathcal{L}_{\text{GAN}}^X$ for discriminator D_X is calculated by comparing x and \hat{x} . **4.** The backward cycle-consistency loss function $\mathcal{L}_{\text{cyc}}^b$ is calculated by comparing \hat{y} to the true target image y . **5.** These loss functions are combined with $\mathcal{L}_{\text{GAN}}^Y$ and $\mathcal{L}_{\text{cyc}}^f$ to calculate the total loss function \mathcal{L} . F and G are then updated to minimize \mathcal{L} . This process is repeated to optimize the neural network.

cycle consistency is achieved when the difference between x' and x is minimized, indicating that the full translation cycle beginning in \mathcal{X} reproduces a close approximation of x ; backward cycle consistency is defined identically for images $y \in \mathcal{Y}$. An optimized CycleGAN will simultaneously minimize the forward and backward cycle consistency error. The cycle-consistency loss function $\mathcal{L}_{\text{cyc}}(G, F)$ we used is defined as

$$\mathcal{L}_{\text{cyc}}(G, F) = \mathbb{E}_{x \sim p_{\text{data}}(x)} [|F(G(x)) - x|_1] + \mathbb{E}_{y \sim p_{\text{data}}(y)} [|G(F(y)) - y|_1], \quad (4)$$

where $|A - B|_1 = \sum_i |A_i - B_i|$ is the pixel-to-pixel L^1 -norm between images A (SDSS) and B (DES). Hence, minimizing $\mathcal{L}_{\text{cyc}}(G, F)$ is equivalent to minimizing the forward and backward cycle consistency error with respect to the L^1 -norm.

The full loss function used for training F and G was

$$\mathcal{L}(G, F, D_X, D_Y) = \mathcal{L}_{\text{GAN}}(G, D_Y, \mathcal{X}, \mathcal{Y}) + \mathcal{L}_{\text{GAN}}(F, D_X, \mathcal{Y}, \mathcal{X}) + \lambda \mathcal{L}_{\text{cyc}}(G, F) \quad (5)$$

for some parameter λ , which describes the relative importance of the optimization of the adversarial and cycle consistency errors. For this work, we set $\lambda = 0.2$.

Image translation using a CycleGAN architecture provides benefit over a traditional GAN by constraining the

allowed mapping functions by ensuring that the discriminator pair F and G are inverses. This benefits the translation between noisy images by making sure that the differences in noise patterns in \mathcal{X} and \mathcal{Y} is taken into account, helping distinguish between the signal and noise more easily after training on many images.

4 RESULTS AND ANALYSIS

Here, we demonstrate that we can transfer information from DES images to their SDSS counterparts, generating synthetic images that are brighter, of higher quality, and have less noise, yet retain the physical information contained within the source image. We begin with a qualitative analysis to understand properties of the reconstructed images, then quantify the brightness and noise level of the image datasets. We then use correlations between the light profiles of the source and reconstructed objects to establish the small-scale differences between the datasets. Finally, we combine this information with comparative quality assessments to establish that the image reconstruction process improves the image quality, brightens objects, and reduces background noise. The robustness of the reconstruction process will be demonstrated by comparing the statistics of the validation and external datasets.

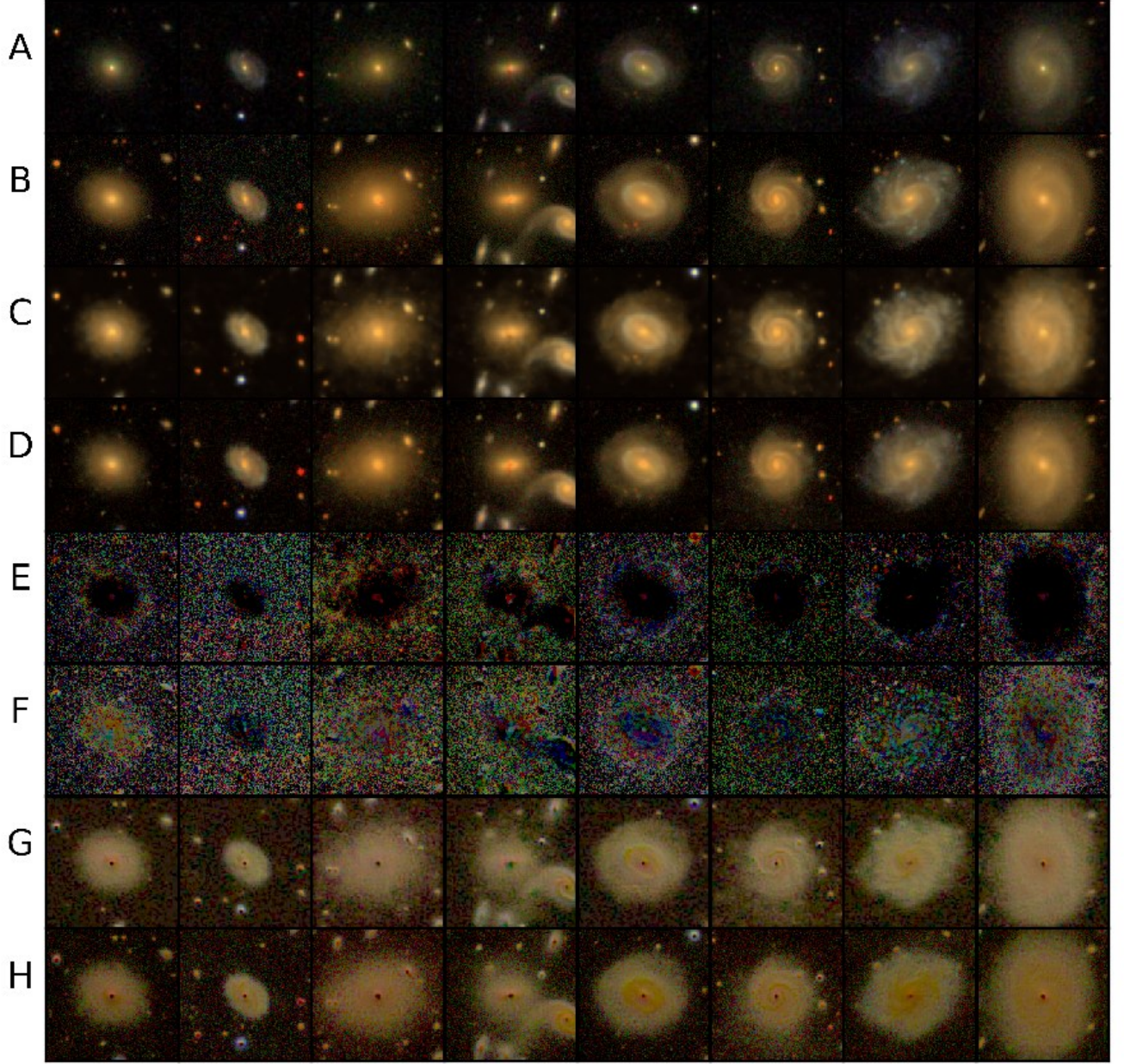


Figure 3: Examples of galaxy images from the validation dataset (from the Stripe82 region) used for validation. Each column shows an SDSS galaxy (row A), its DES counterpart (row B), and the DES image reconstruction by the AECNN (row C) and CycleGAN (row D) methods. AECNN and CycleGAN residuals (reconstruction - DES) are shown in rows E and F respectively, while the AECNN and CycleGAN pixel-to-pixel brightness increases (reconstruction - SDSS) are shown in rows G and H, respectively. **Note that to increase visibility, images in rows E, F, G and H were artificially enhanced with a power law transform ($P_i \rightarrow P'_i = (P_i/255)^\gamma$ each pixel P_i).** In rows E and F, $\gamma = 0.3$, while in rows G and H, $\gamma = 0.5$. Additional galaxy samples can be found in Appendix A.

4.1 Qualitative Analysis

Figure 3 shows several examples of false images generated by the neural networks paired with their corresponding SDSS and DES images from the overlap region. These images were selected to demonstrate the wide variety of galaxy types and structures included in the validation sample which were not including during the training. Row A contains images from

the SDSS catalog; the corresponding DES images are located in row B. Rows C and D contain the reconstructed AECNN and CycleGAN images, respectively. We can observe that the DES images and the synthetic images in rows C and D are remarkably similar, where the small differences come from the the lack of structure resolution of the reconstructed objects.

Qualitatively, the reconstructed images are blurrier

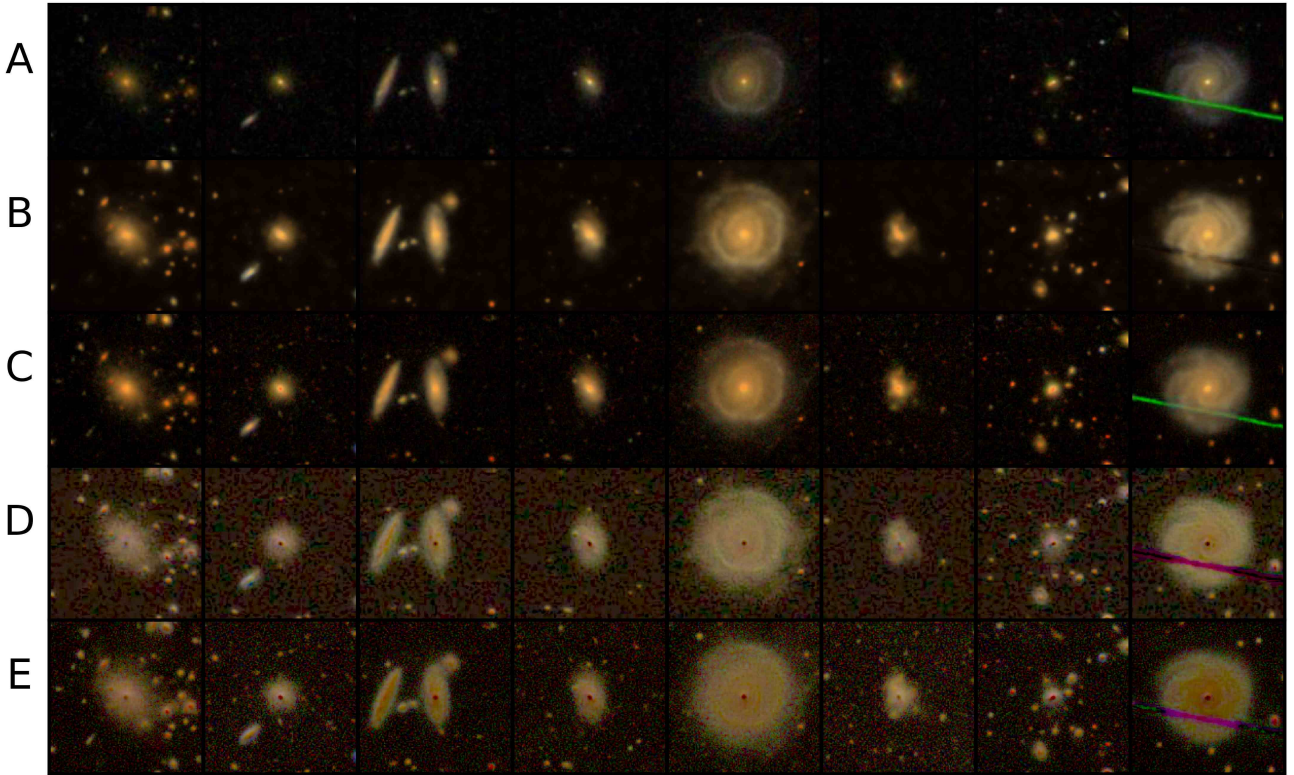


Figure 4: Examples of galaxy images from the external dataset (from outside of the Stripe82 overlap region). Each column shows an SDSS galaxy (row A) and the DES image reconstruction by the AECNN (row B) and CycleGAN (row C) methods. The AECNN and CycleGAN pixel-to-pixel brightness increases (reconstruction - SDSS) are shown in rows D and E, respectively. **Note that to increase visibility, images in rows D and E were artificially enhanced with a power law transform ($P_i \rightarrow P'_i = (P_i/255)^\gamma$ for each pixel P_i , where $\gamma = 0.5$).** Additional galaxy samples can be found in Appendix A.

than the corresponding DES images. However, images reconstructed by both the models are brighter and have higher S/N than the SDSS images. Image residuals for the AECNN and CycleGAN reconstructions are shown in rows E and F, respectively. These show the pixel-to-pixel brightness differences between the reconstructed and DES images; note that these images were artificially enhanced using a power law transform ($P_i \rightarrow P'_i = (P_i/255)^\gamma$ for each pixel P_i ; in rows E and F, $\gamma = 0.3$, while in rows G and H, $\gamma = 0.5$). This was done so that the residual structure was visible; otherwise the differences are too hard to observe. It appears that both neural networks isolated and enhanced the galaxy signal while affecting the background minimally or try to reduce the noise. Both networks were also able to distinguish between separate structures on each image; this is particularly evident in the second column.

Rows G and H show the pixel-to-pixel brightness increase provided by the AECNN and CycleGAN reconstructions relative to the corresponding SDSS galaxies, respectively. Qualitatively, the AECNN reconstructions are brighter than the CycleGAN images, and provided greater amplification to the internal structure of each galaxy. Interestingly, both networks consistently amplified the galaxy center more than other regions. This amplification was not exclusive to the central galaxy; rather, it was present in most

regions the network identified as a signal region. Other example galaxies are included in Appendix A.

Figure 4 shows examples of images from the external dataset (from outside of the Stripe82 region). These images are generally of lower quality; however, both reconstruction models succeeded in selecting and amplifying the objects of interest with little effect on the background, even maintaining much of the small-scale detail of the images (particularly in the fourth and seventh columns). As in Figure 3, the reconstructions generally increased the spatial extent of objects in the image. Notably, the AECNN reconstruction appears to have removed an artifact from the SDSS image in the final column; this phenomenon is discussed in greater detail in Section 4.4.

4.2 Dataset Properties

Here, we quantify the brightness and quality of images from each dataset to use as baseline comparison metrics between the original input SDSS images, the DES target images, and the reconstructions.

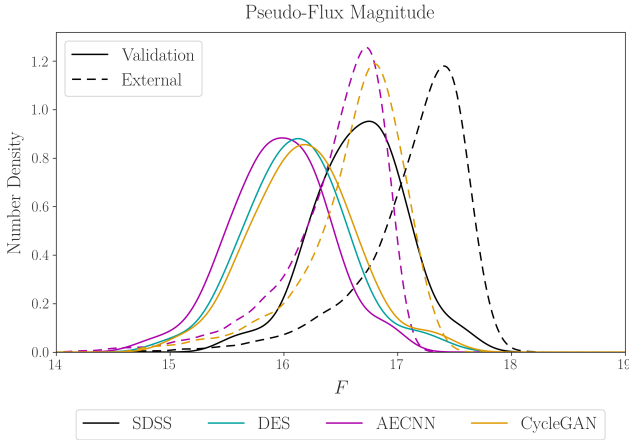


Figure 5: Pseudo-flux magnitudes (defined in Eqn. (6)) for the validation and external data. SDSS images tend to be fainter than the DES counterparts. Both reconstruction models increased the brightnesses of the images.

Pseudo-Flux Magnitude

In this work we have used the R, G, B images from SDSS and DES to test our architectures. Image brightness was quantified using the average pseudo-flux magnitude F of each image. We refer to F as the ‘‘pseudo-flux magnitude’’ because, while F does not represent the physical flux magnitude (our images consisted solely of R, G, B band values), it acts as a proxy for this quantity due to the similarities between the two measurements. The pseudo-flux magnitude F was defined by

$$F = 30 - 2.5 \log \left(\sum_{r_i < r_{\max}} \beta_i \right) \quad (6)$$

$$= 30 - 2.5 \log \beta^{\circ}.$$

Here, the pixel brightness β_i describes the average of the red, green, and blue channel values in P_i and β° is the total pixel brightness contained within an aperture of radius $r_{\max} = 75$ pix. A constant factor (zero point) of 30 was added to approximate the appearance of a physical magnitude distribution.

Gaussian kernel density estimates (KDEs) for histograms of the pseudo-flux magnitudes are shown in Figure 5. All datasets have similarly shaped pseudo-flux magnitude distributions; however, the SDSS distributions are shifted towards fainter magnitudes, indicating that both reconstruction models increased the brightnesses of the SDSS images. Furthermore, the similarity between the DES and reconstruction distributions implies that the brightness was increased through image-to-image translation and that the CycleGAN reconstructions matched the brightness of DES images. This pattern is also reflected in the external data. The skew in the external data distributions arises from the lower quality and brightness of the SDSS dataset. In addition, the training and validation sets were selected so that their properties matched those of the DES images, which led to an implicit selection bias in those distributions that created additional skew.

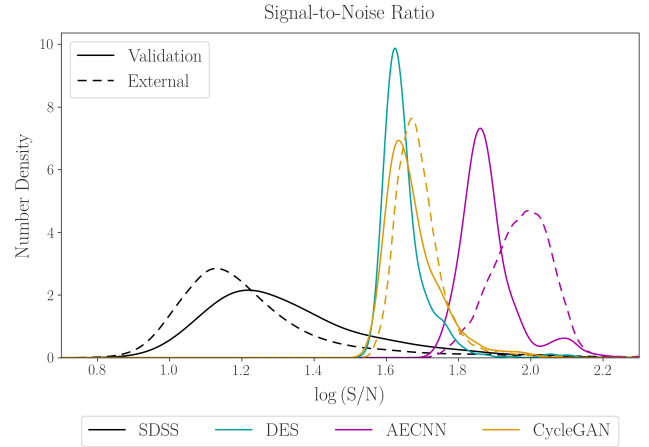


Figure 6: KDEs of the histograms of the mean S/N (defined in Eqn. (7)) for the validation and external data. Both reconstruction models were effective at increasing the S/N.

Signal-to-Noise Ratio

As metric for image quality, we measured the average signal-to-noise ratio (S/N) of images in each dataset. In Figure 6, we show KDEs for histograms of the mean S/N, which is defined as

$$S/N = \frac{\mu_{\beta}^{\circ}}{\sigma_{\beta}^{\circ}}, \quad (7)$$

where μ_{β}° (σ_{β}°) is the mean (standard deviation) of the pixel brightness β for pixels within a radius of $r_{\max} = 75$ pix.

For both datasets, the mean S/N for the SDSS data was lowest. The CycleGAN distribution matched the DES distribution closely, while the S/N for the AECNN distributions was higher. This indicates that, on average, both reconstruction models were effective at boosting the signal amplitude, and that the S/N for the CycleGAN reconstructions nearly matched that of the DES images.

4.3 Luminosity Profile

In Section 4.2, we showed that the average pseudo-flux magnitudes of the reconstructed images closely corresponded with their DES counterparts. Now, we will compare the pseudo-luminosity profiles of the objects in these images to characterize the structure of the objects themselves.

The pseudo-luminosity profile, $\frac{dF}{dS}$, which is analogous to the luminosity profile in observed data, is defined by

$$\frac{dF(r)}{dS} = \frac{1}{2\pi r \Delta r} \sum_{r_i \in \text{Ann}(r)} F_i \quad (8)$$

$$= \frac{F_{\text{Ann}(r)}}{2\pi r \Delta r}$$

where $F_{\text{Ann}(r)}$ is the total flux contained within an annulus-shaped aperture $\text{Ann}(r)$ with central radius r and area $2\pi r \Delta r$, where $\Delta r = 1$ pix

Plots of the pseudo-luminosity profile for the validation and external datasets are shown in Figure 7. In both datasets, the pseudo-luminosity profile for each image set

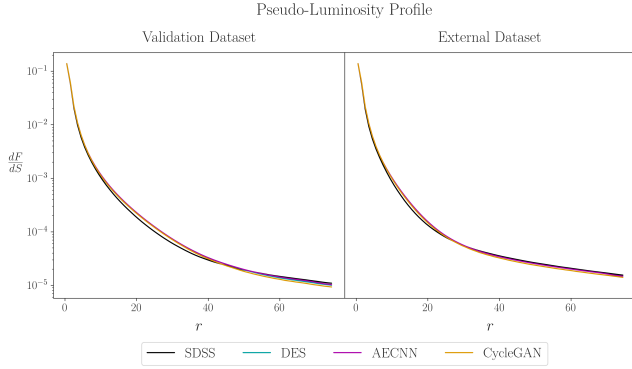


Figure 7: Pseudo-luminosity profiles $\frac{dF}{dS}$ for the validation (left) and external (right) data; $\frac{dF}{dS}$ is defined in Eqn. (8). DES, AECNN, and CycleGAN images each had an increase in average pixel brightness relative to SDSS, with DES and CycleGAN being nearly equivalent and AECNN gaining more than DES and CycleGAN.

was similar. In both the external and validation datasets, the profiles from each image set were similar to one another; however, from the pseudo-flux magnitude results (Figure 5), the reconstructions were generally brighter than their SDSS counterparts. This implies that the reconstructions improved the brightness quality of the SDSS images without losing information about the object’s brightness profile distribution.

4.4 Image Quality Comparison

As shown in Section 4.2, the DES and reconstructed image brightnesses are similar to one another, and in 4.3, we show that the brightness increase provided by the reconstruction has little effect on the radial profiles of the objects. Now, we will characterize how effective each reconstruction model is at amplifying the image signal, reducing background noise, improving image quality, and retaining the morphological information contained within the original image. We also highlight several notable images from the external dataset that show that AECNN reconstructions may help remove image artifact.

The mean structural similarity index (MSSIM) (Zhou Wang et al. 2004) is a method used to compare image quality that takes into account differences in brightness, sharpness, and small-scale features. The MSSIM is defined by the product of the luminance index ℓ , contrast index c , and cross-correlation index s . For a pair of images \mathbf{X} and \mathbf{Y} , where each respective entry \mathbf{X}_{ij} and \mathbf{Y}_{ij} is the pixel brightness β_{ij} of pixel P_{ij} , let \mathbf{x}_{ij} (\mathbf{y}_{ij}) be an 11×11 window centered around pixel x_{ij} (y_{ij}). After smoothing \mathbf{x}_{ij} (\mathbf{y}_{ij}) by an 11-tap Gaussian filter, define ℓ , c , and s as

$$\begin{aligned} \ell(\mathbf{x}_{ij}, \mathbf{y}_{ij}) &= \frac{2\mu_x\mu_y + C_1}{\mu_x^2 + \mu_y^2 + C_1} \\ c(\mathbf{x}_{ij}, \mathbf{y}_{ij}) &= \frac{2\sigma_x\sigma_y + C_2}{\sigma_x^2 + \sigma_y^2 + C_2}, \\ s(\mathbf{x}_{ij}, \mathbf{y}_{ij}) &= \frac{2\sigma_{xy} + C_2}{2\sigma_x\sigma_y + C_2}. \end{aligned} \quad (9)$$

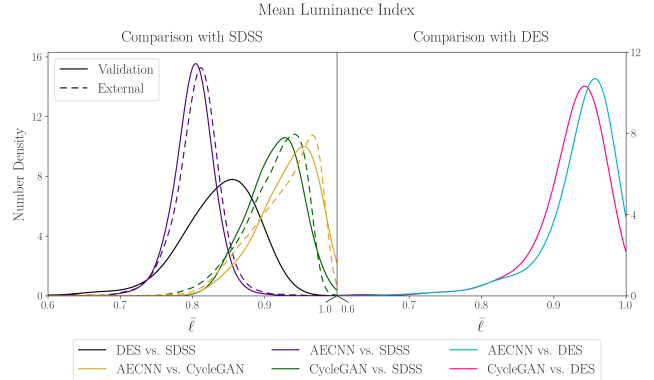


Figure 8: Mean luminance index $\bar{\ell}$ (defined in Eqn. (9)) for the validation and external data. $\bar{\ell}$ describes the similarities in brightness between two images at small scales (~ 10 pix). The robustness of the method is indicated by the similarities in the validation and external distributions in the left-hand plot. In the right-hand plot, both reconstruction models increased $\bar{\ell}$ equally, indicating that, at small scales, the brightness increase provided by the two models were similar. This supports the conclusions drawn from the pseudo-flux magnitude (see Fig. 5).

Then structural similarity index SSIM can be calculated as

$$\begin{aligned} \text{SSIM}(\mathbf{x}_{ij}, \mathbf{y}_{ij}) &= \ell(\mathbf{x}_{ij}, \mathbf{y}_{ij}) c(\mathbf{x}_{ij}, \mathbf{y}_{ij}) s(\mathbf{x}_{ij}, \mathbf{y}_{ij}) \\ &= \frac{(2\mu_x\mu_y + C_1)(2\sigma_{xy} + C_2)}{(\mu_x^2 + \mu_y^2 + C_1)(\sigma_x^2 + \sigma_y^2 + C_2)}, \end{aligned}$$

Here, μ_x (μ_y) is the mean of \mathbf{x}_{ij} (\mathbf{y}_{ij}), σ_x^2 (σ_y^2) is the variance of \mathbf{x}_{ij} (\mathbf{y}_{ij}), σ_{xy} is the covariance, $C_1 = (0.01R_D)^2$, and $C_2 = (0.03R_D)^2$ are stabilization constants for which R_D is the dynamic range of the image (in our case, $R_D = 255$). Then the MSSIM is defined by

$$\text{MSSIM} = \frac{1}{N_P^2} \sum_{i,j}^{N_P} \text{SSIM}(\mathbf{x}_{i,j}, \mathbf{y}_{i,j}) \quad (10)$$

and the mean luminance, contrast, and cross-correlation indices ($\bar{\ell}$, \bar{c} , and \bar{s} , respectively) are defined similarly.

KDEs of histograms for $\bar{\ell}$, \bar{c} , \bar{s} , and MSSIM for the overlap and external data are shown in Figures 8, 9, 10, and 11, respectively.

As the SDSS galaxies are substantially different in brightness and radii, it is not valid to use $\bar{\ell}$, \bar{c} , \bar{s} , and MSSIM as image quality metrics for DES/SDSS and reconstruction/SDSS image pairs. However, if the reconstruction process is robust, the distributions for DES/SDSS pairs and reconstruction/SDSS pairs should be consistent in the validation and external datasets. Hence, we will use reconstruction/DES and reconstruction/reconstruction measurements to quantify the reconstruction quality and reconstruction/SDSS measurements as metrics for robustness.

The mean luminance index $\bar{\ell}$ is a measure of the differences in the pixel-to-pixel brightness of two (smoothed) images. The reconstruction/DES distributions for $\bar{\ell}$ were all very similar in the validation dataset, and both peaked close

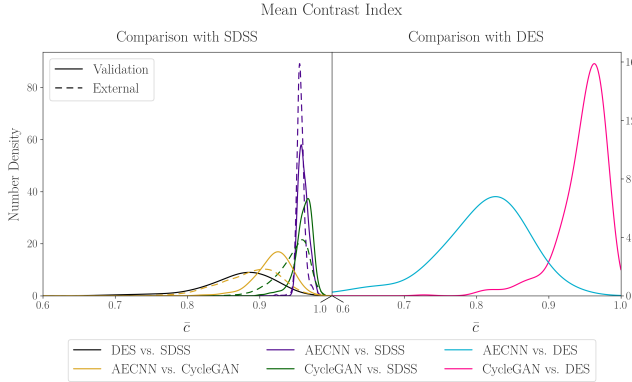


Figure 9: Mean contrast index \bar{c} (defined in Eqn. (9)) for the validation and external data. \bar{c} describes the relative sharpness of two images at small scales (~ 10 pix). The robustness of the method is indicated by the similarities in the validation and external distributions in the left-hand plot. In the right-hand plot, \bar{c} was generally lower for the AECNN reconstructions than for the CycleGAN reconstructions, implying that the AECNN images were generally blurrier than the CycleGAN images. This confirms the qualitative observations about the images described in Section 4.1 (see Fig. 3).

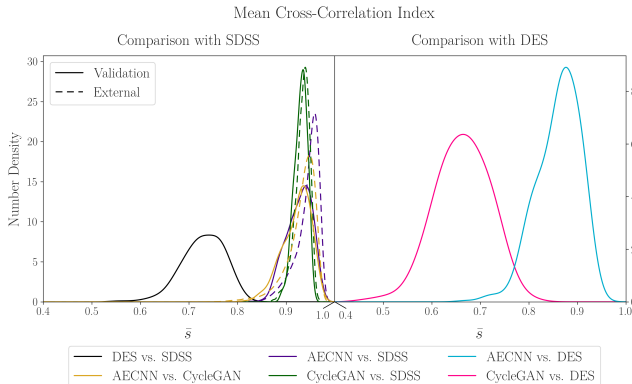


Figure 10: Mean cross-correlation index \bar{s} (defined in Eqn. (9)) for the validation and external data. \bar{s} describes the similarities between the structure of two images at small scales (~ 10 pix), providing a measure of the faithfulness of the reconstruction. The robustness of the method is indicated by the similarities in the validation and external distributions in the left-hand plot. In the right-hand plot, \bar{s} was generally lower for the CycleGAN reconstructions than for the AECNN reconstructions, implying that the AECNN architecture more accurately recreated small-scale details of the DES images, providing a more accurate reconstruction of the morphological properties of the image.

to $\bar{\ell} = 1$. This implies that the brightnesses of the reconstructed images were similar to that of their DES counterparts. The brightness quality of the reconstructions relative to their SDSS counterparts were extremely similar to one another in both the validation and external distributions, implying that both were equally effective at increasing the image brightnesses. Finally, the AECNN/CycleGAN distributions both peaked near $\bar{\ell} = 1$, showing that the brightnesses of the reconstructed images were similar to one another at small length scales. This agrees with our analysis of the pseudo-flux magnitude measurements (Section 4.2).

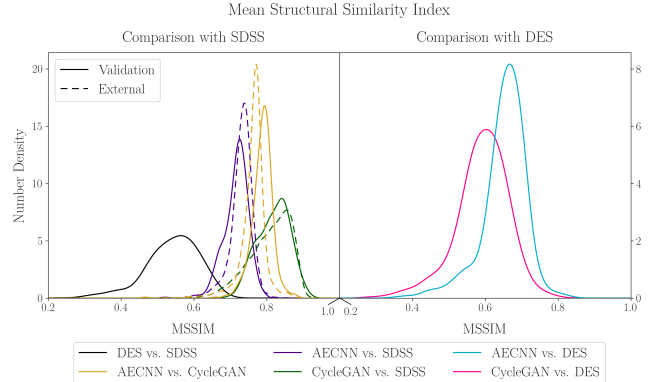


Figure 11: Mean structural similarity index (defined in Eqn. (10)) for the validation and external data. The MSSIM, which is the mean of the product of ℓ , c , and s , provides a metric for the overall relative image quality. The robustness of the method is indicated by the similarities in the validation and external distributions in the left-hand plot. From the right-hand plot, we can see that the overall quality of the AECNN images was similar to that of the DES images, while the quality of the CycleGAN reconstructions was further removed from that of the DES images.

nesses of the reconstructed images were similar to one another at small length scales. This agrees with our analysis of the pseudo-flux magnitude measurements (Section 4.2).

The mean contrast index \bar{c} describes the average difference in sharpness between small cut-outs of image pairs after normalizing for the sharpness of each individual image. For the validation data, the \bar{c} distributions for CycleGAN/DES peaked very close to $c = 1$, implying that the sharpness of the DES images was transferred to the SDSS images via the reconstruction process. However, the AECNN/DES distribution confirms that the AECNN images were blurrier than the DES and CycleGAN images.

The mean cross-correlation index \bar{s} is a measure of the deviations in the small-scale structure between two images; large values of \bar{s} indicate that, after normalizing for the brightness and sharpness, the morphological features of the images at small scales are similar to (strongly correlated with) one another. The \bar{s} distributions for the validation data indicates that the AECNN reconstructions are more closely correlated with their DES counterparts at small scales than the CycleGAN reconstructions. This implies that AECNN reconstruction preserves more information at small scales than CycleGAN.

The combination of these quantities yielded the MSSIM distributions seen in Figure 11. This metric indicates that the AECNN images were of overall higher quality than the CycleGAN reconstructions; however, the breakdown in terms of $\bar{\ell}$, \bar{c} , and \bar{s} suggests that the reconstruction methods provide differing benefits. Specifically, CycleGAN reconstructions are generally sharper than their AECNN counterparts, while AECNN reconstructions preserve more information at small scales in the image.

For each metric, the external AECNN/CycleGAN and reconstruction/SDSS distributions are similar to their validation data counterpart. This implies that the AECN and CycleGAN reconstructions shared the same qualities with

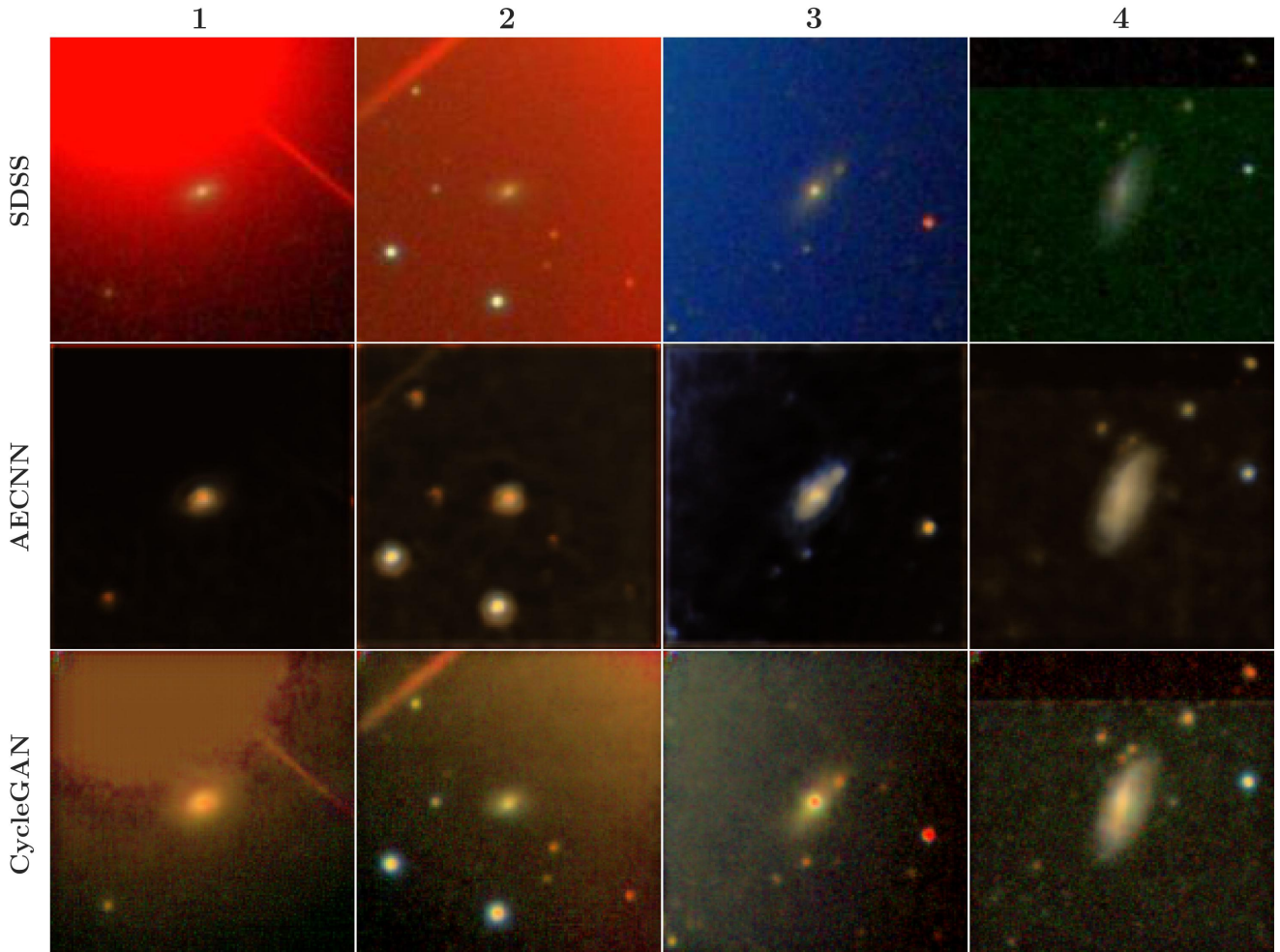


Figure 12: A selection of several notable objects from the external dataset. In each of these images, it appears that the AECNN reconstructions may have removed large artifacts from the image.

their SDSS counterparts in both the validation and external datasets, demonstrating that the reconstruction process adapted to the lower-quality external data to generate accurate false image representations of DES objects in the external data. The $\bar{\ell}$ distributions had a particularly strong correspondence, implying that the brightness information translation was especially robust.

Finally, we would like to highlight several unique images from the external dataset; these are shown in Figure 12. These images were found through visual inspection of images with the lowest reconstruction/SDSS $\bar{\ell}$, \bar{c} , \bar{s} , and/or MSSIM values in the external dataset.

Each image in 12 is heavily corrupted by artifacts; however, the AECNN reconstructions appear to have removed these artifacts at the cost of blurring the objects in the image. The CycleGAN reconstructions, however, fail to consistently remove these artifacts, though do succeed in amplifying the brightness of these objects. Though the use of AECNN reconstruction as a method of artifact removal is beyond the scope of this study, these images suggest that this application warrants further research.

5 CONCLUSIONS

In this work, we demonstrated the viability of robust cross-survey galaxy image translation using neural networks and generative models. Using the pseudo-flux magnitude (Section 4.2) and mean luminance index $\bar{\ell}$ (Section 4.4), we show that the average brightnesses of the reconstructions more closely match DES images than their SDSS source images while preserving the structural information contained within the source galaxy (Section 4.3). In Section 4.2, we also demonstrated that the signal-to-noise ratio of the false images closely correlates with that of the DES images. Together, these imply that our method can be used to improve image brightness and signal strength using image-to-image translation. In Section 4.4, we discuss the pros and cons of each reconstruction method using the mean contrast index \bar{c} and cross-correlation index \bar{s} . We found that CycleGAN reconstructions were sharper, while AECNN reconstructions more accurately reproduced the structure of DES galaxies at length scales on the order of several pixels at the cost of being slightly blurrier. Finally, we highlighted several instances in which the reconstructions appear to have removed large artifacts. The robustness of our method was demon-

strated by performing image reconstructions on images from the external region from the SDSS catalog, which contains objects without a DES counterpart. Though these images were fainter and had lower S/N than images from the overlap region (Stripe82), the large- and small-scale statistics of these image reconstructions were similar to those in the overlap region, implying that the reconstruction process accurately created DES representation of these objects. This fact have potentially great implications as we could grab every single galaxy from SDSS and recompute all of their quantities using DES reconstructions and by increasing the S/N ration we can achieve much better statistics and lower errors in different models for galaxy populations for example.

The reconstruction pipeline we developed solely constitutes a initial exploration, but the efficiency and robustness of the reconstruction process shows promise as a method for generating or improving survey data. All quantities calculated were derived solely from the mean of the R , G , B channel values of survey images; however, we anticipate that similar methods could be used for the generation of false images with physical observables consistent with those of survey images. In particular, we expect that methods similar to ours could be used to generate images with realistic flux profiles. In addition, our methodology could be expanded to enable cross-wavelength or band-to-band translation. A neural network could be trained with a feature set containing fewer bands than the target dataset, generating a map between each pair of bands in the training and target data. The trained network could be used to supplement survey data by generating realistic reconstructions of image data in frequency bands not probed by that survey which is something we will explore in future work.

6 ACKNOWLEDGMENTS

This material is based upon work supported by the National Science Foundation Graduate Research Fellowship Program under Grant No. DGE — 1746047. M. Carrasco Kind has been supported by NSF Grant AST-1536171.

Author contribution

B. Buncher: Data analysis, figure creation, writing, and editing.
A. N. Sharma: AI model creation, data collection, figure creation, writing, and editing.
M. Carrasco Kind: Oversight, data collection, writing, and editing.

Softwares Used

This research made us of `matplotlib` (Hunter 2007), `numpy` (Oliphant 2006; Van Der Walt et al. 2011), `scikit-image` (Van der Walt et al. 2014), `SciPY` (Virtanen et al. 2019), and `seaborn` (Waskom et al. 2017).

This research made use of `Astropy`,⁴ a community-

⁴ <http://www.astropy.org>

developed core Python package for Astronomy (Astropy Collaboration et al. 2013; Price-Whelan et al. 2018).

This research made use of `Photutils`, an `Astropy` package for detection and photometry of astronomical sources (Bradley et al. 2019).

Appendices

A ADDITIONAL IMAGE SAMPLES

Here, we show additional examples of SDSS, DES, and reconstructed images from the validation dataset similar to Figure 3. They were selected to provide examples of objects with a variety of types, brightnesses, and extents.

The rows in each image represent the following quantities:

- (A) SDSS representation
- (B) DES representation
- (C) AECNN reconstruction
- (D) CycleGAN reconstruction
- (E) AECNN residuals (AECNN - DES)
- (F) CycleGAN residuals (CycleGAN - DES)
- (G) AECNN gain (AECNN - SDSS)
- (H) CycleGAN gain (CycleGAN - SDSS)

Note that to increase visibility, images in rows E, F, G and H were artificially enhanced with a power law transform (see text for more details).

REFERENCES

- Abazajian K. N., et al., 2009, *ApJS*, **182**, 543
- Abbott T. M. C., et al., 2018, *ApJS*, **239**, 18
- Ahumada R., et al., 2020, *ApJS*, **249**, 3
- Astropy Collaboration et al., 2013, *A&A*, **558**, A33
- Bepler T., Zhong E. D., Kelley K., Brignole E., Berger B., 2019, arXiv e-prints, p. [arXiv:1909.11663](https://arxiv.org/abs/1909.11663)
- Bowen I. S., Vaughan A. H., 1973, *Appl. Opt.*, **12**, 1430
- Bradley L., et al., 2019, `astropy/photutils`: v0.6, doi:10.5281/zenodo.2533376, <https://doi.org/10.5281/zenodo.2533376>
- Cortese L., Catinella B., Janowiecki S., 2017, *ApJL*, **848**, L7
- Durugkar I. P., Gemp I., Mahadevan S., 2016, CoRR, abs/1611.01673
- Flaugher B., Diehl H. T., Honscheid K., et al., 2015, *AJ*, **150**, 150
- Gunn J. E., et al., 2006, *Astron. J.*, **131**, 2332
- Holtzman J., Harrison T., Coughlin J., 2010, *Advances in Astronomy*, 2010
- Hunter J. D., 2007, Computing in Science & Engineering, **9**, 90
- Isola P., Zhu J.-Y., Zhou T., Efros A. A., 2017, CVPR
- Jiang L., et al., 2014a, *ApJS*, **213**, 12
- Jiang L., et al., 2014b, *Astrophys. J. Suppl.*, **213**, 12
- Lample G., Zeghidour N., Usunier N., Bordes A., Denoyer L., Ranzato M., 2017, arXiv e-prints, p. [arXiv:1706.00409](https://arxiv.org/abs/1706.00409)
- Lanusse F., Mandelbaum R., Ravanbakhsh S., Li C.-L., Freeman P., Poczos B., 2020, arXiv e-prints, p. [arXiv:2008.03833](https://arxiv.org/abs/2008.03833)
- Li L., Huang H., Jin X., 2018, in 2018 9th International Conference on Information Technology in Medicine and Education (ITME). pp 39–42, doi:10.1109/ITME.2018.00020
- Lupton R., Blanton M. R., Fekete G., Hogg D. W., O’Mullane W., Szalay A., Wherry N., 2004, *PASP*, **116**, 133
- Oliphant T., 2006, NumPy: A guide to NumPy, USA: Trelgol Publishing

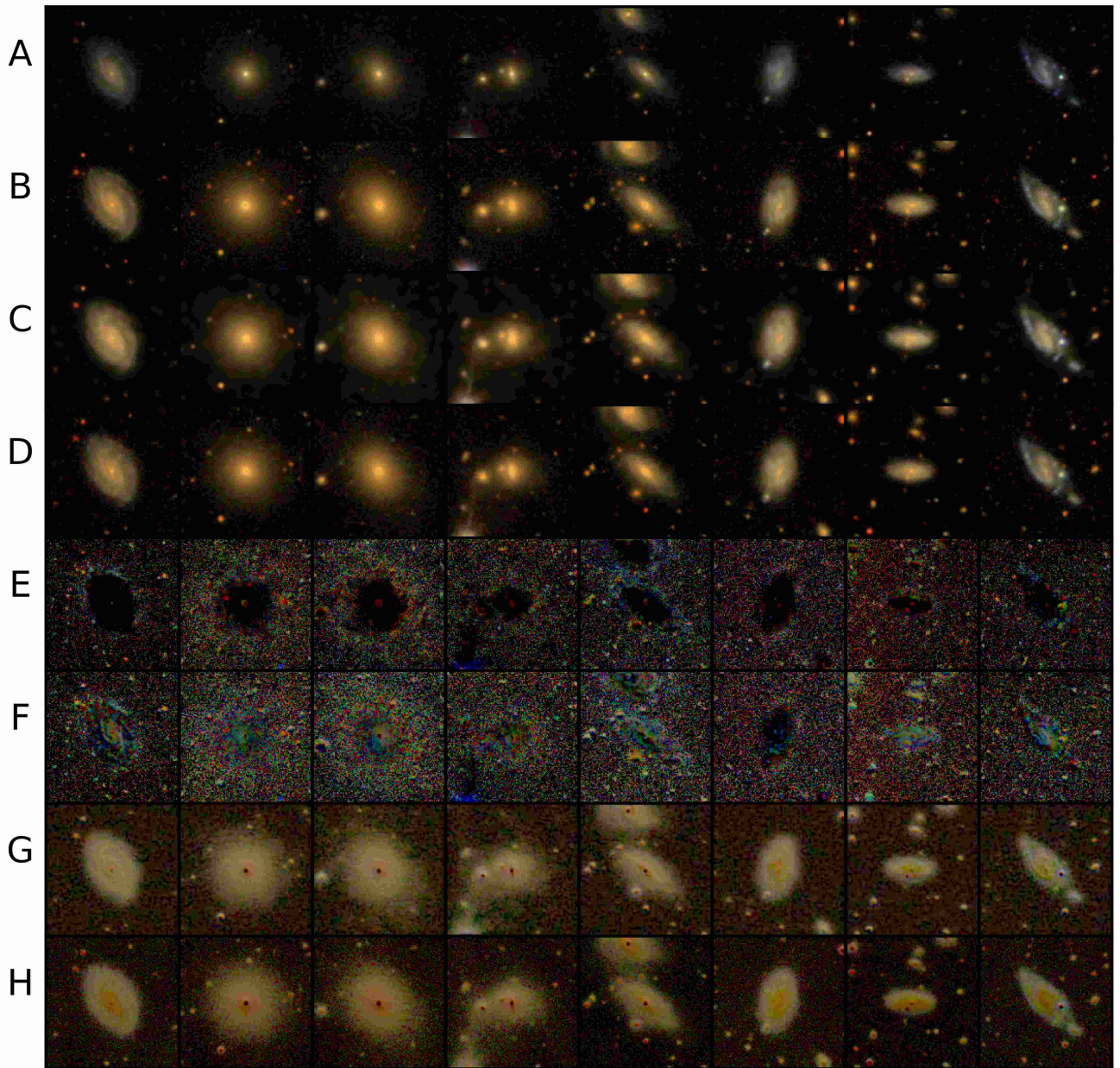


Figure 13: Additional examples of source, target, and reconstructed images from the validation dataset. Equivalent to Figure 3. Note the enhancement for the difference images in E, F, G and H for clarity.

Padmanabhan H., Loeb A., 2020, arXiv e-prints, [p. arXiv:2002.01489](#)
 Perarnau G., van de Weijer J., Raducanu B., Álvarez J. M., 2016, arXiv e-prints, [p. arXiv:1611.06355](#)
 Price-Whelan A. M., et al., 2018, *AJ*, **156**, 123
 Regier J., McAuliffe J., Prabhat M., 2015a, in NIPS Workshop: Advances in Approximate Bayesian Inference.
 Regier J., Miller A., McAuliffe J., Adams R., Hoffman M., Lang D., Schlegel D., Prabhat 2015b, arXiv e-prints, [p. arXiv:1506.01351](#)
 Rowe B. T. P., et al., 2015, *Astronomy and Computing*, **10**, 121
 Schawinski K., Turp M. D., Zhang C., 2018, *A&A*, **616**, L16
 Smith M. J., Geach J. E., 2019, *MNRAS*, **490**, 4985
 Van Der Walt S., Colbert S. C., Varoquaux G., 2011, Computing

in Science & Engineering, **13**, 22
 Van der Walt S., Schönberger J. L., Nunez-Iglesias J., Boulogne F., Warner J. D., Yager N., Gouillart E., Yu T., 2014, *PeerJ*, **2**, e453
 Virtanen P., et al., 2019, arXiv e-prints, [p. arXiv:1907.10121](#)
 Wang Y., et al., 2019, *MNRAS*, **490**, 5722
 Waskom M., et al., 2017, mwaskom/seaborn: v0.8.1 (September 2017), [doi:10.5281/zenodo.883859](#), <https://doi.org/10.5281/zenodo.883859>
 Zeiler M. D., 2012, arXiv e-prints, [p. arXiv:1212.5701](#)
 Zhou Wang Bovik A. C., Sheikh H. R., Simoncelli E. P., 2004, *IEEE Transactions on Image Processing*, **13**, 600
 Zhu J.-Y., Park T., Isola P., Efros A. A., 2017, arXiv e-prints, [p. arXiv:1703.10593](#)

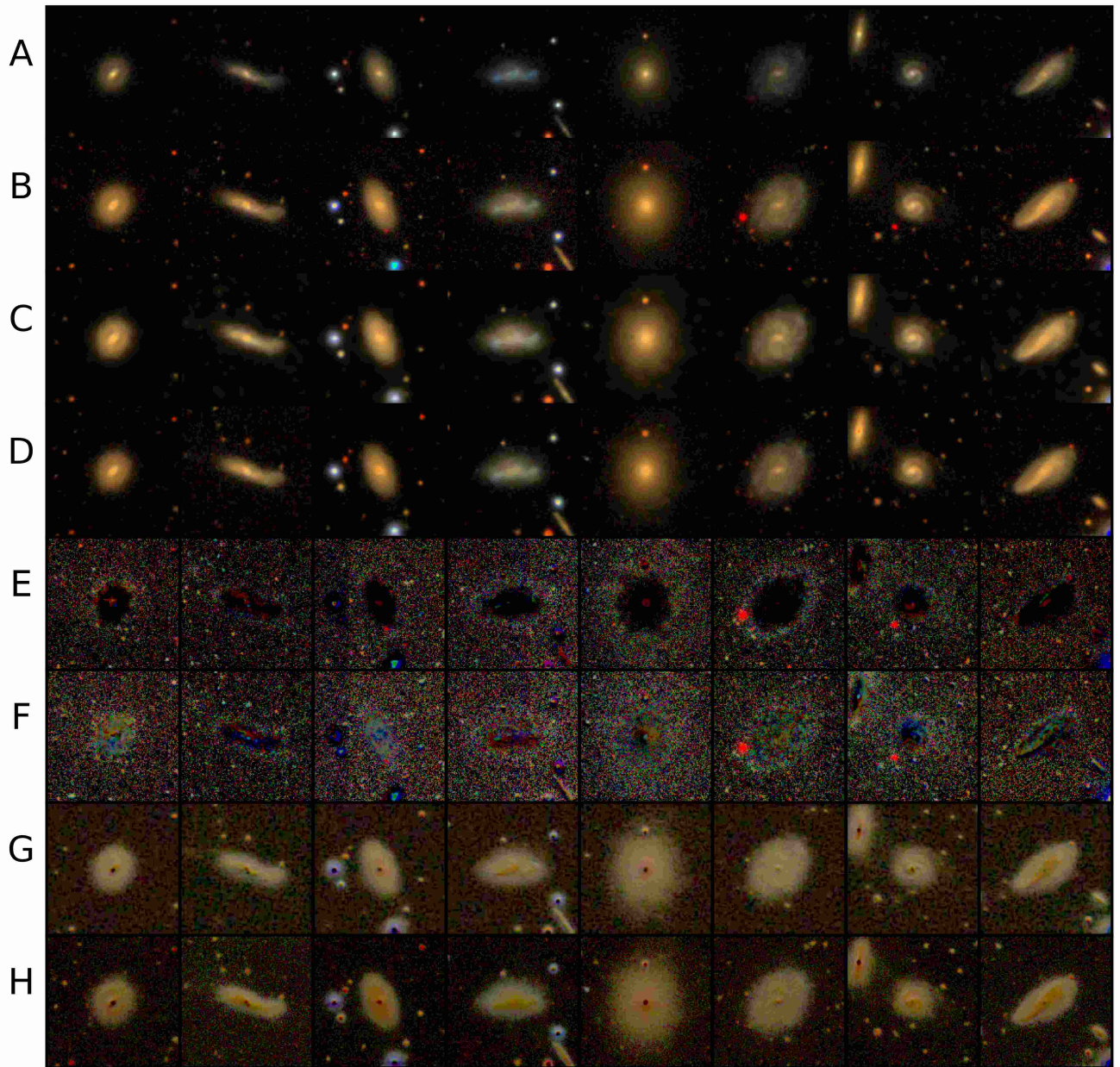


Figure 14: Additional examples of source, target, and reconstructed images from the validation dataset. Equivalent to Figure 3. Note the enhancement for the difference images in E, F, G and H for clarity.

This paper has been typeset from a $\text{\TeX}/\text{\LaTeX}$ file prepared by the author.

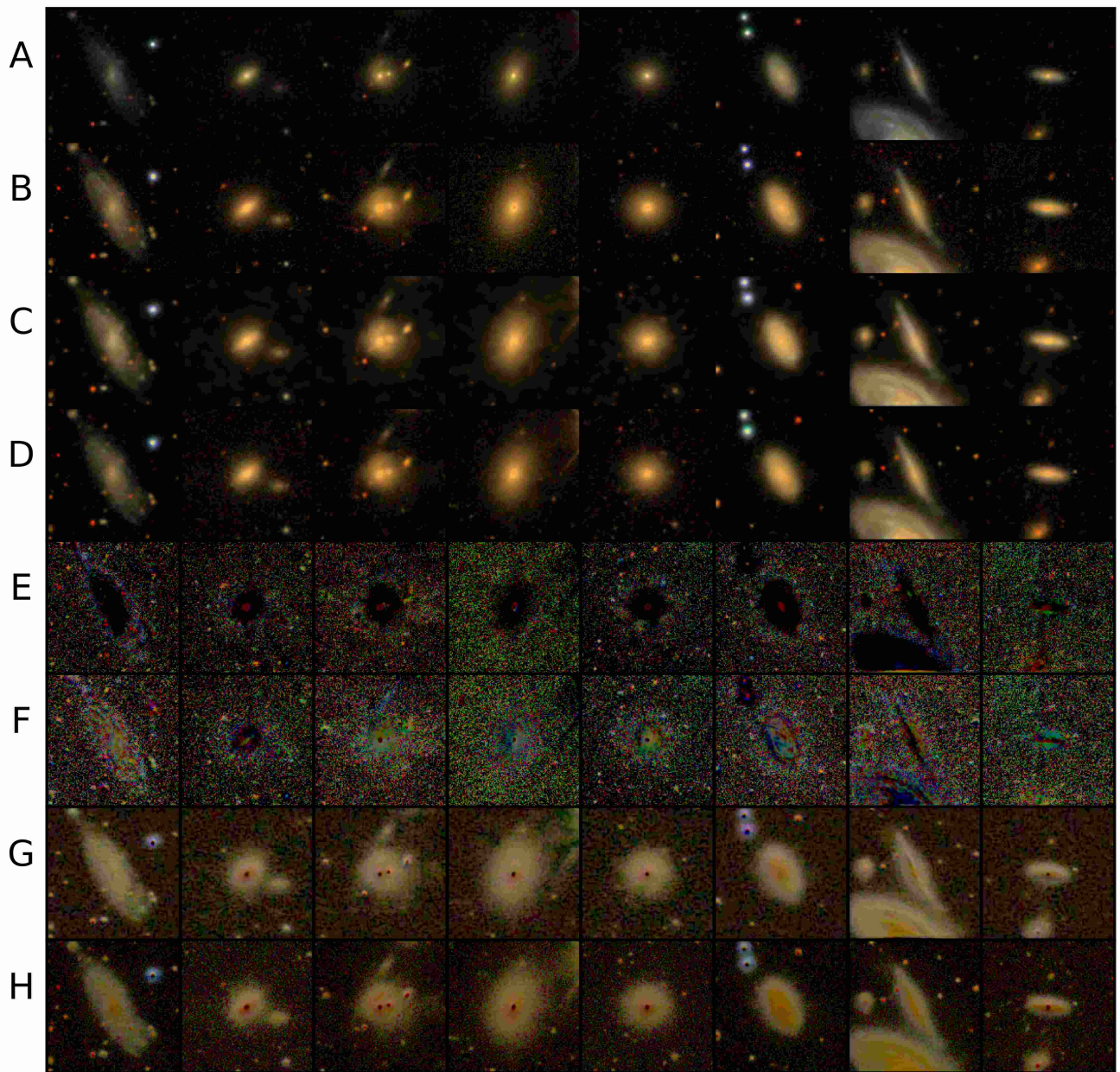


Figure 15: Additional examples of source, target, and reconstructed images from the validation dataset. Equivalent to Figure 3. Note the enhancement for the difference images in E, F, G and H for clarity

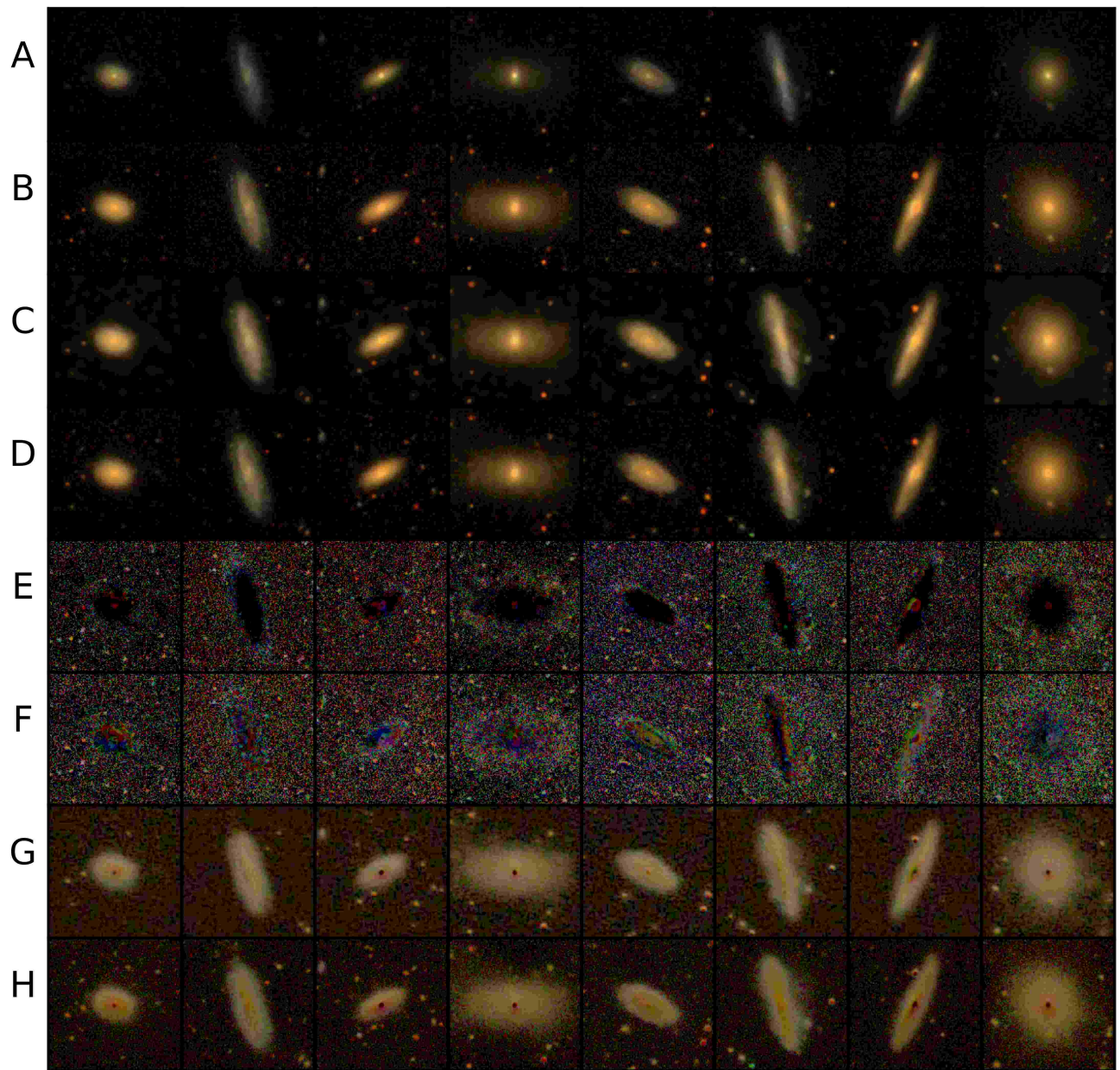


Figure 16: Additional examples of source, target, and reconstructed images from the validation dataset. Equivalent to Figure 3. Note the enhancement for the difference images in E, F, G and H for clarity

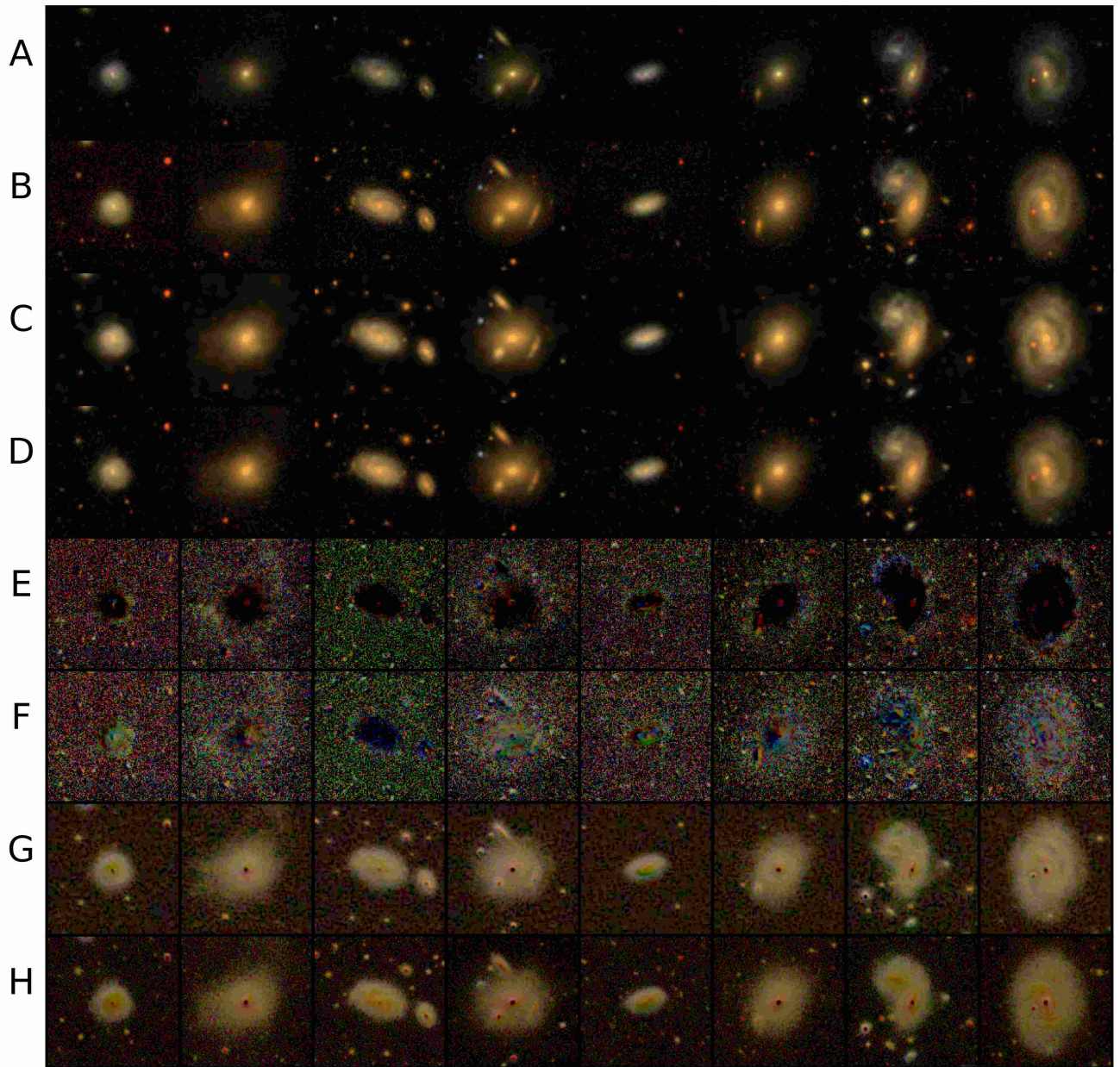


Figure 17: Additional examples of source, target, and reconstructed images from the validation dataset. Equivalent to Figure 3. Note the enhancement for the difference images in E, F, G and H for clarity

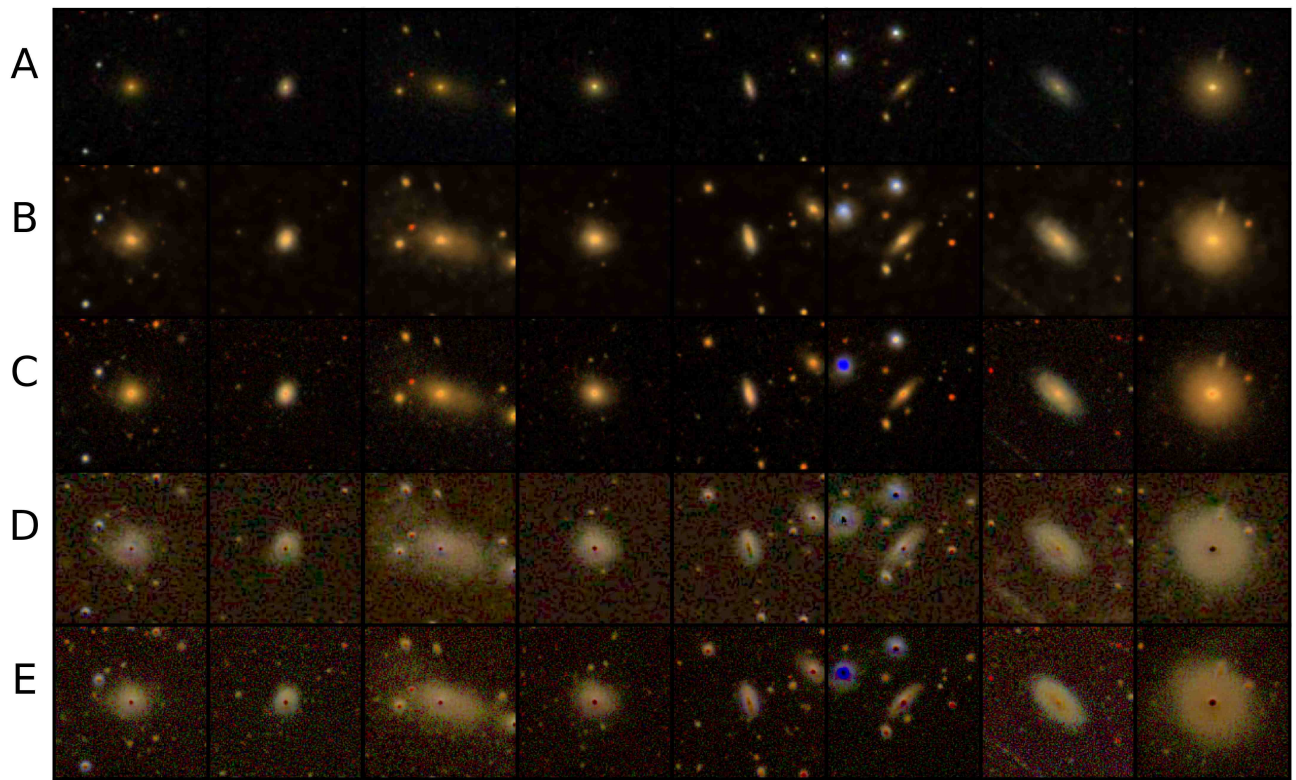


Figure 18: Additional examples of source and reconstructed images from the external dataset where there is no DES counterpart. Equivalent to Figure 4. Note the enhancement for the difference images in D, E for clarity